



Promoted Cu-Fe₃O₄ catalysts for low-temperature water gas shift reaction: Optimization of Cu content



Han Yan, Xue-Tao Qin, Yue Yin, Yun-Fei Teng, Zhao Jin, Chun-Jiang Jia*

Key Laboratory for Colloid and Interface Chemistry, Key Laboratory of Special Aggregated Materials, School of Chemistry and Chemical Engineering, Shandong University, Jinan 250100, China

ARTICLE INFO

Keywords:

Cu-based catalyst
Water gas shift
Mutual interaction
Structure-function relation

ABSTRACT

Promoted Cu-Fe₃O₄ catalysts for water gas shift (WGS) reaction are synthesized via an aerosol-spray self-assembly (ASSA) method. The structure changes of fresh, reduced and used catalysts are characterized by multiple techniques including scanning and transmission electron microscope (SEM and TEM), *ex-situ/in-situ* X-ray diffraction (XRD) and N₂-adsorption. By using temperature-programmed reduction (TPR) under different atmospheres (H₂/CO) and X-ray photoelectron spectroscopy (XPS), the interaction between Cu and Fe species has been confirmed, and highly dispersive Cu⁰ has been further identified as the active phase. The Cu-Fe interaction helps stabilize and greatly improve the dispersion of Cu⁰ and thus enhances the WGS conversion. The addition of Fe also facilitates the adsorption of CO and H₂O, as demonstrated by diffuse reflectance infrared Fourier transform spectroscopy (DRIFTS) of *in-situ* mode. The Cu_{0.3}Fe_{0.7}O_x catalyst exhibits very high catalytic activity and a tri-component Cu-Fe₃O₄-Al₂O₃ catalyst shows even better WGS conversion and stability.

1. Introduction

The water gas shift (WGS) reaction is an exothermic reversible reaction kinetically favored at higher temperature and thermodynamically favored at lower temperature. It is a crucial reaction in various industrial procedures. During the industrial hydrogen production processes, in order to achieve higher hydrogen production from fossil fuels with less energy consumption, WGS reactors at different temperature ranges with different catalysts are usually applied. The high-temperature shift (HTS) reaction is performed with Fe-based catalysts at around 350–450 °C, while the low-temperature shift (LTS) reaction is performed with Cu-based catalysts at around 190–250 °C [1–3]. Besides, in recent years, the rapid development of proton-exchange membrane fuel cells technique requires clean H₂ sources since trivial CO will poison the Pt electrodes. With the help of Au- or Pt-based catalysts, WGS reaction can reduce CO concentration to the ppm level [4–6]. Thus, the deeper development of WGS catalysts, especially LTS catalysts, is very likely to benefit the industrial fields, such as industrial hydrogen production and new energy sources.

Cu-based catalysts for LTS process have been widely applied because of the high catalytic activity [7–11]. Besides, due to the economic considerations, copper catalysts have also been evaluated as alternatives of the noble metals catalysts. Considerable efforts have been made to clarify the impacts of different factors on the properties of Cu-

based LTS catalysts, such as the nature of supports [12–15], the influence of promoters [16–18] and the effect of bimetallic synergy [19–21]. The determination and evolution of active sites and reaction mechanism have also been studied using various techniques [22–25]. However, the enhancement of catalytic performance of Cu-based LTS catalysts through adding non-precious promoters, is still challenging. Among the various candidates, Fe promoter has been reported to effectively improve the CO conversion and stability for WGS Cu-based catalysts [26–31]. Cu-Fe-O catalysts has exhibited promising prospect in the applications for WGS reaction.

Former reported Cu-Fe-O WGS catalysts have mainly focused on Fe-Cu-Al-O [32–37] or CuFe₂O₄ [24,38–40] catalysts, which serve as a replacement for toxic Fe-Cr-O HTS catalysts. Systematic study of Cu-Fe-O LTS catalysts is still rarely reported. Among the limited reports, Yahirō et al. [26] found that Al₂O₃ is a proper support for Cu-FeO_x, due to the formation of highly dispersive metallic Cu⁰. Lin et al. [29,30] studied the influence of preparation methods and precipitants, announcing that co-precipitation method with KOH precipitant gave the best catalyst. Wu and Chen et al. [31] studied the impact of tiny amount of Fe addition on Cu/SiO₂ catalysts, and Fe promoter was found to improve WGS activity and stability. In these reports, where supported catalyst with 10–12 wt% Cu [26,31] and bulk materials with 1:4 Cu-Fe molar ratio [28–30] are studied, the catalytic activity is limited due to the low Cu content. The research and pursuit for highly active Cu-Fe-O catalysts

* Corresponding author.

E-mail address: jiacj@sdu.edu.cn (C.-J. Jia).

are not covered, and the optimal Cu-Fe ratio has not been determined yet. Besides, the role that Fe promoter plays and the Cu-Fe interaction, that affects the physicochemical and catalytic properties in the Cu-Fe-O catalysts, still requires further study.

Herein, we report bulk Cu- Fe_3O_4 WGS catalysts with different Cu-Fe molar ratio. The catalysts are facilely synthesized by an aerosol-spray self-assembly (ASSA) method [41–43]. The $\text{Cu}_{0.3}\text{Fe}_{0.7}\text{O}_x$ catalyst exhibits very high WGS activity during the measurement of catalytic performance. Systematic investigations demonstrate that the addition of Fe component significantly improves the dispersion of Cu-species, which results in better reducibility and CO adsorption due to the enhanced Cu-Fe interaction. Moreover, the Fe introduction facilitates the adsorption H_2O under catalytic conditions, and thus improves the WGS activity. The optimization of Cu content proves that excessive amount of Cu results in sintering and deactivation of the catalyst, while catalysts with low Cu content suffer from CO poisoning and limited Cu^0 . A tri-component Cu- Fe_3O_4 - Al_2O_3 catalyst shows superiority over Cu- Fe_3O_4 catalyst in the activity and stability tests, where the inhibition of Cu^0 sintering has a great impact.

2. Experimental

2.1. Catalysts preparation

2.1.1. Materials

All materials used for catalysts preparation were bought from commercial suppliers without any reform. The metal nitrates ($\text{Al}(\text{NO}_3)_3 \cdot 9\text{H}_2\text{O}$, 99.0%, $\text{Fe}(\text{NO}_3)_3 \cdot 9\text{H}_2\text{O}$, 99.5%, $\text{Cu}(\text{NO}_3)_2 \cdot 3\text{H}_2\text{O}$, 98.0%) were obtained from Tianjin Kermal Factory. F127 ($M_w = 12\,000\text{ g mol}^{-1}$), the copolymer as templating agent was bought from Sigma-Aldrich.

2.1.2. Catalysts preparation

Scheme 1 displays the whole procedure for catalysts preparation, namely, the ultrasonic spray method. In a typical synthesis, metal nitrates (4 mmol in total) and 0.4 g of triblock copolymer F127 are dissolved in 60 mL of absolute ethanol. The formed precursor is sonicated for 10 min to get the dark brown solution, which is then atomized in an ultrasonic humidifier (30 W, 1.5 MHz). N_2 is used as carrier gas to introduce the generated spray into the tube furnace. While in the furnace (preheated to 400 °C), the metal nitrates decompose and self-assembly. The products are spherical metal oxides, obtained in the collector and

stored overnight at 60 °C. Afterwards, the products go through 4 h of calcination at 400 °C in air with the ramping rate of 1 °C min⁻¹. Cu- Fe_3O_4 - Al_2O_3 catalysts are prepared using the same procedure by also adding aluminum nitrate. The synthesized catalysts are nominated as $\text{Cu}_a\text{Fe}_b\text{O}_x$ or $\text{Cu}_a\text{Fe}_b\text{Al}_c\text{O}_x$, of which the letters mean the molar ratio of each element. For example, $\text{Cu}_{0.3}\text{Fe}_{0.7}\text{O}_x$ means the molar ratio of Cu and Fe is 3:7 and $\text{Cu}_{0.3}\text{Fe}_{0.6}\text{Al}_{0.1}\text{O}_x$ indicates the molar ratio of Cu, Fe and Al is 3:6:1.

2.2. Catalysts characterization

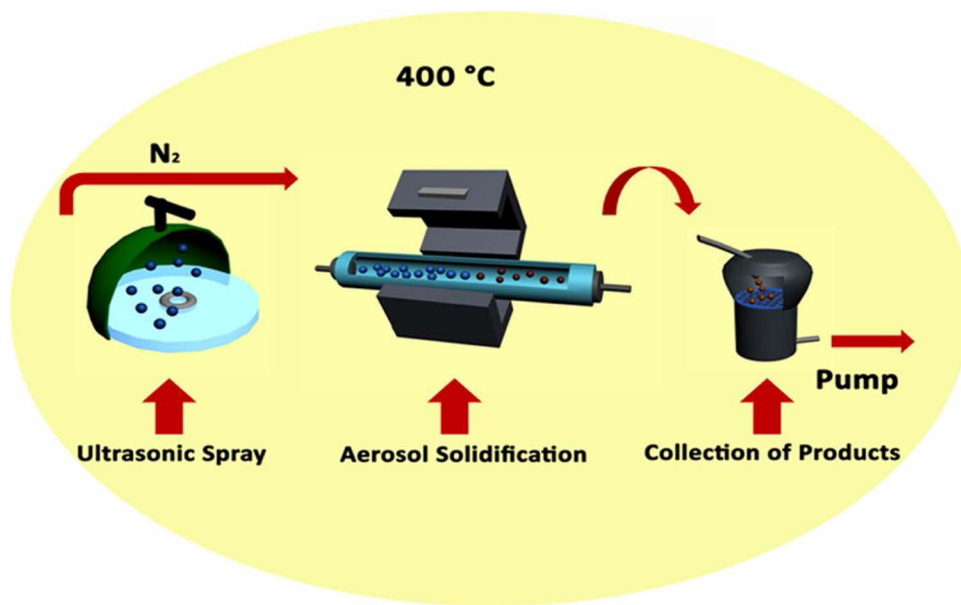
The images of transmission electron microscope (TEM) are derived by using a JEOL JEM-2100 microscope (200 kV). The images of scanning electron microscope (SEM) are taken on a Zeiss SUPRA 55 scanning microscope, of which the acceleration voltage was 5.0 kV. The element mapping results and metal content of each catalyst are derived from the EDX spectroscopy analysis equipped to the scanning microscope.

X-ray diffraction (XRD) experiments, both *ex-situ* and *in-situ* modes, are conducted *via* a powder diffractometer from PANalytical B.V. X'pert3 (Cu K_α radiation, $\lambda = 0.15406\text{ nm}$), using the accelerating voltage and current of 40 kV and 40 mA. A PIXcel^{1D} detector is chosen for obtaining *ex-situ* XRD patterns in the 2θ range of 10–90°. An Anton Paar XRK900 *in-situ* chamber is applied for deriving *in-situ* XRD patterns. For the *in-situ* XRD experiments, the ceramic sample holder is loaded with roughly 100 mg of sample. The reaction chamber is heated up to 300 °C for 0.5 h in 5% H_2 /Ar gas as an activation process. After cooling down in pure nitrogen, the chamber is heated in a 5% CO/N_2 gas mixture. The XRD patterns are collected at room temperature and 50 °C higher ever since 150 °C to 400 °C. The heating rate of the chamber and the gas flow rate are set as 30 °C min⁻¹ and 30 mL min⁻¹, respectively.

The analysis of X-ray photoelectron spectroscopy (XPS) is operated on an Axis Ultra imaging photoelectron spectrometer from Kratos, Japan(225 W, Al K_α radiation). The core level binding energies are exactly determined by calibrating the spectrometer with C 1s at 284.8 eV.

Builder surface area analyzer (SSA-4200) is used for the nitrogen sorption measurements at 77 K. The samples are degassed at 200 °C for 6 h under vacuum before measurements. The calculation of specific surface area for each sample is based on the Brunauer-Emmett-Teller (BET) method.

Scheme 1. Schematic of the typical aerosol-assisted self-assembly approach (ASSA) equipment.

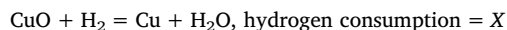


Temperature-programmed reduction with hydrogen (H₂-TPR) and CO (CO-TPR) is performed by using a Builder PCSA-1000 adsorption instrument. A thermal conductivity detector (TCD) and online mass spectrometer (Ametek LC-D200 M) are chosen to analyze the outlet gases, respectively. The catalysts are sieved and 30 mg are stuffed in the quartz reactor. Before measurement, every sample is treated in pure O₂ at 300 °C for 0.5 h to degas the adsorbed gases. The reduction gas compositions (30 mL min⁻¹) are 5% H₂/Ar or 5% CO/Ar gas mixture. The measurement are accomplished by reducing the samples from room temperature to 900 °C with a ramping rate of 10 °C min⁻¹.

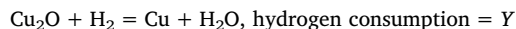
The outlet gases of temperature-programmed desorption by CO₂ (CO₂-TPD) and temperature-programmed surface reaction (TPSR) are analyzed with Ametek LC-D200 M mass spectrometer. During the activation process, 200 mg of each catalyst are reduced at 300 °C in 5% H₂/Ar (30 mL min⁻¹) for 30 min. After activation, the catalyst is flushed under He at room temperature for 1 h. For CO₂-TPD, the samples are flushed with 5% CO₂/Ar (30 mL min⁻¹) for 30 min followed by purging under helium at 50 °C for another 1 h to remove physisorbed gas. The TPD measurement is started by heating from 100 °C to 900 °C under helium flow. The ramping rate is set as 10 °C min⁻¹. For TPSR, the samples are flushed with 2%H₂O, 2% CO₂/Ar (30 mL min⁻¹) and heated from 120 °C to 400 °C with ramping rate of 10 °C min⁻¹.

The Cu dispersion is determined by performing selective N₂O adsorption at 50 °C. The Catalysts first go through H₂-TPR procedure described above until 300 °C. The catalyst bed is then cooled to 50 °C and flushed with helium. The metallic copper atoms at surface are selectively oxidized in a 20% N₂O/N₂ gas mixture (30 mL min⁻¹) at 50 °C for 0.5 h. After that, the catalysts are purged with He again and cooled to room temperature, followed by launching another H₂-TPR run to 500 °C. The hydrogen consumption is acquired through integral of reduction peak area. The calculation of Cu dispersion and active Cu surface area (S_{cu}) are based on the calculation reported before [44,45].

All copper atoms went through total reduction in the first TPR run:



Cu₂O at surface oxidized by N₂O from metallic copper atoms shall be reduced in the second TPR run:



The Cu dispersion (D) and active Cu surface (S_{cu}) were derived as:

$$D = (2 \times Y/X) \times 100\%$$

$$S_{\text{cu}} = D \times N_{\text{av}} \times X_{\text{Cu}} / (A_{\text{Cu}} \times 1.4 \times 10^{19}),$$

where N_{av} is Avogadro's constant. X_{cu} represents the Cu metal content (determined by EDX spectroscopy in our study). A_{cu} is the atomic weight of Cu.

In-situ Diffuse reflectance infrared Fourier transform spectroscopy (DRIFTS) characterization is conducted on a BrukerVertex 70 spectrometer. The mercury-cadmium-telluride (MCT) detector is applied and the cooling is achieved by liquid nitrogen. The *in-situ* cell is a diffuse reflectance cell (Harrick system) rigged with CaF₂ windows. In a typical steady test, the powder sample (ca. 20 mg) is pre-reduced in 5% H₂/Ar for 30 min at 300 °C as activation process and cooled down to 200 °C under pure N₂ (30 mL min⁻¹). Then a background spectrum is collected *via* 32 scans at 4 cm⁻¹ resolution. The reaction gas with 2%CO/2% H₂O/96%N₂ is introduced into the *in-situ* chamber (30 mL min⁻¹). The IR profiles are recorded continuously for 30 min to obtain equilibrium results. As for CO sorption tests, 2%CO/98%N₂ and pure N₂ are used and the data are collected every minute. All DRIFTS results analysis is conducted by using OPUS software.

2.3. Catalytic tests

WGS reaction is tested using a fixed-bed reactor (d = 1 cm). A thermocouple is mounted on top of the catalyst bed and connected with

a PID temperature controller. 100 mg of catalyst are loaded and pre-treated with 5% H₂/Ar gas mixture for 30 min at 300 °C. A 2.2%CO/N₂ stream (56 cm³ min⁻¹) is fed to mix with water vapor in the reactor to perform the reaction. The CO and H₂O are in a 1:7 feed ratio with total GHSV of 42,000 cm³ g⁻¹ h⁻¹. Heating of reactor begins from 150 °C to 400 °C as 50 °C per step. The flowing pipeline of the reactor is twined with heating belts to prevent water condensation. All the outlet gases are analyzed online by a Gasboard 3500 IR spectroscopy (WuhanSifang Company, China). The CO conversion of WGS is derived from the equation: CO conversion = CO_{converted}/CO_{input}.

In order to evaluate the catalytic stability, the WGS reaction is kept at 250 °C for 140 h and the conversion data are continuously recorded. The GHSV for long-term stability tests is either maintained at 42,000 cm³ g⁻¹ h⁻¹ or elevated to higher values with CO/H₂O in a 1:7 feed ratio. The apparent activation energy (E_a) for WGS reaction is obtained at 160 – 320 °C, while CO conversion less than 15% is regulated by tuning reaction temperature, the loading of the catalysts and stream flow rate. The calculation of reaction rate (r_{CO}) and turnover frequency (TOF) of WGS follow the expression reported by D.I. Kondarides et al. [46].

$$r_{\text{CO}} = F \times \text{CO converted}/W,$$

where r_{CO} is the CO reaction rate of WGS reaction (mol g⁻¹ s⁻¹). F is the whole flow rate of the stream (mol s⁻¹). CO_{converted} is CO converted concentration and W is the catalyst mass of the (g).

$$\text{TOF} = r_{\text{CO}} \times A_{\text{Cu}} / (D \times X_{\text{Cu}}),$$

Where TOF is the CO turnover frequency of WGS reaction (s⁻¹), defined as moles of CO molecules converted per second per surface Cu atom. A_{cu} is the atomic weight of Cu. D represents the dispersion of Cu and X_{cu} represents the Cu metal content (determined by EDX in our study).

3. Results

3.1. Structure properties

Fig. 1 illustrates the XRD results of the fresh, reduced and used Cu₂O catalysts. The patterns for freshly prepared catalysts are exhibited in **Fig. 1a**. Monoclinic CuO and rhombohedral hematite are observed as the dominating crystalline phase. After H₂ reduction or WGS reaction, as shown in **Fig. 1b** and c, most CuO component is reduced to cubic metallic Cu⁰, and hematite is reduced to cubic Fe₃O₄. The existence of CuO and Cu₂O in **Fig. 1b** and 1c may arise from the incomplete reduction or the re-oxidation when exposed in the air. The sharpening of Cu peaks after H₂ reduction or WGS reaction indicates the growth of Cu particles. The calculated particle sizes of CuO and metallic Cu⁰ refer to Sherrer equation. The corresponding d_{CuO} and d_{Cu} are exhibited in **Table 1** and **Fig. 2a**, showing the Fe introduction is able to effectively reduce the size of Cu species. The calculated d_{CuO} is reduced from 19.9 nm to 6.6 nm for the pure CuO sample and Cu_{0.3}Fe_{0.7}O_x, respectively. As for Cu_{0.1}Fe_{0.9}O_x, since the Cu content is very low, the CuO reflection is too weak for accurate evaluation. The Cu dispersion is also improved with the addition of Fe component, which agrees well with the varying trend of d_{CuO} and d_{Cu}, as shown in **Fig. 2a**.

The isotherms of nitrogen adsorption measurements for the catalysts are depicted in **Fig. S1**. In **Fig. S1a**, the sorption isotherms of fresh pure CuO sample exhibits a type II adsorption-desorption isotherm, which suggests the sample is nonporous. The other six samples exhibit type IV adsorption-desorption isotherms, indicating the existence of mesopores. **Fig. 2b** demonstrates the varying trend of surface area as a function of Cu content. With the elevating Fe content, the BET specific surface area of the fresh samples increases, and all catalysts lose most of their surface area after H₂ reduction or reaction. The loss is probably caused by the mesopores blockage arising from the sintering at high temperature.

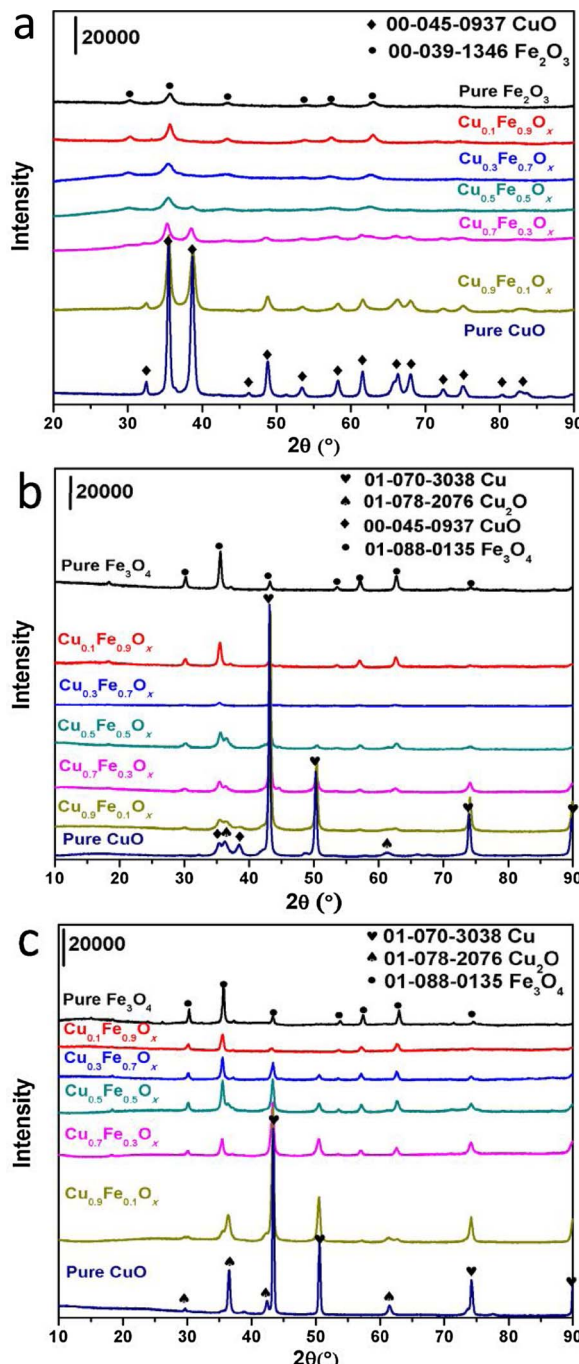


Fig. 1. X-ray diffraction (XRD) patterns of (a) fresh catalysts produced via ASSA; (b) catalysts after H_2 reduction treatment (reduced samples); (c) catalysts after temperature dependent catalytic tests (used samples).

Besides, it is also noteworthy in Fig. 2b that the Cu^0 surface area (S_{Cu}) for pure CuO increased from 0.7 to $16.8 \text{ m}^2 \text{ g}^{-1}$ when mixed with 10 mol% Fe. The Cu^0 surface area continues to increase with more Fe content until that of $\text{Cu}_{0.3}\text{Fe}_{0.7}\text{O}_x$ reaching $32.1 \text{ m}^2 \text{ g}^{-1}$, the largest value in the Cu- Fe_3O_4 catalysts. The trend of Cu^0 surface area can be reflected by a continuous increase of Cu dispersion with more Fe content (Fig. 2a and Table 1). However, for $\text{Cu}_{0.1}\text{Fe}_{0.9}\text{O}_x$, the Cu^0 surface area drops to $13.6 \text{ m}^2 \text{ g}^{-1}$ even though the Cu dispersion was as high as 19.4%. Such a decrease may arise from the insufficient amount of surface Cu due to the low Cu content in $\text{Cu}_{0.1}\text{Fe}_{0.9}\text{O}_x$.

The morphology and surface texture of the catalysts prepared via ASSA are studied with scanning electron microscope (SEM). According

to Fig. S2, all freshly prepared catalysts give the morphology of microspheres with the diameters ranging from 0.1 to $2 \mu\text{m}$. The size distribution corresponds well to the dimension of the droplets from the generated spray [47]. As displayed in Fig. S2, with the increasing amount of Fe molar ratio, the microspheres show more spherical and relatively smooth surfaces. In comparison, the SEM micrograph of pure Fe_2O_3 exhibits uniform spherical and mesoporous structure (Fig. S2g), while the microspheres of pure CuO sample are anomalous and loosely packed (Fig. S2a). Moreover, the morphology of the catalysts has a clear change after the H_2 reduction treatment. As illustrated in Fig. 3, for catalysts with high Cu content ($\text{Cu}_{0.9}\text{Fe}_{0.1}\text{O}_x$ and $\text{Cu}_{0.7}\text{Fe}_{0.3}\text{O}_x$), the sintering of catalysts is so severe that the spherical structure is almost lost. Comparatively, the surface texture is better preserved with the increasing amount of Fe molar ratio (Fig. 3d and e). The element mapping micrograph of $\text{Cu}_{0.3}\text{Fe}_{0.7}\text{O}_x$ is given in Fig. S3. All elements including Cu, Fe and O are uniformly distributed in the microsphere. These results suggest that all the components in the Cu- Fe_3O_4 catalysts can be uniformly dispersed, which is very helpful in the further surface study.

X-ray photoelectron spectroscopy (XPS) analysis is performed to investigate the surface structure and chemical state of fresh Cu-Fe-O catalysts. Fig. 4 exhibits the Cu and Fe 2p spectra. The changes of surface bonding with varying Cu-Fe molar ratio are examined by measuring the shift of 2p core electrons binding energies (BE). In Fig. 4a, the absence of peaks at 932 eV for all samples suggests no detectable metallic Cu^0 or Cu^+ is present, and the strong satellite peaks located between 944–945 eV further indicate that the Cu species on the surface exist as 2+ valence state. The BE of Cu 2p_{3/2} gives the value of 933.6 eV for pure CuO sample (Table 2). This value differs slightly to the 933.9 eV BE of neat CuO material reported by Scott et al. [7], which may ascribe to the different preparation methods of the catalysts. It is noteworthy that with the introduction of Fe component, the Cu 2p_{3/2} maxima shifts continuously from 933.9 eV for pure CuO to 932.2 eV for $\text{Cu}_{0.1}\text{Fe}_{0.9}\text{O}_x$ (Fig. 4a and Table 2). Meanwhile, as shown in Fig. 4b, the BE of Fe 2p_{3/2} gives the value of 710.6 eV for pure Fe_2O_3 sample. Though low in electron density, the characteristic satellite peak at about 718 eV proves Fe_2O_3 rather than Fe_3O_4 is formed at the surface [32–35]. The chemical state of Fe_2O_3 corresponds well to the XRD patterns in Fig. 1a, showing hematite phase for pure Fe_2O_3 sample. Moreover, the Fe 2p_{3/2} maxima shifts continuously from 710.6 eV to 711.2 eV as the Cu content increases (Fig. 4b and Table 2). The corresponding trends of peaks shift provide firm evidence of the interaction between Cu^{2+} and Fe^{3+} species, which infers an electron density increase in Cu nucleus as Fe content elevated.

The bulk compositions of reduced Cu- Fe_3O_4 catalysts, which derives from Energy-dispersive X-ray (EDX) spectroscopy, are listed as weight ratio in Table 1. The reason of performing EDX analysis in examining compositions of materials prepared via ASSA has been described before [48]. Table 2 displays the relative elemental ratios of Cu and Fe on the surface. The ratios are calculated from the intensity ratios of XPS normalized by the atomic sensitivity factors. The molar ratio in Table 2 suggests the actual surface loadings of cation are very close to the nominal values, and thus proves that ASSA was a reliable protocol to give precise compositional control of the catalysts.

3.2. TPR analysis

Temperature-programmed reduction (TPR) experiments are accomplished to further examine the interaction and redox property of the Cu- Fe_3O_4 catalysts. The corresponding results are shown in Fig. 5a. As can be seen, a single large peak between 200 and 400 °C for pure CuO shall be ascribed to the full reduction of bulk CuO to metallic Cu^0 . For pure Fe_2O_3 , the small peak centered at 280 °C shall be attributed to the reduction of Fe_2O_3 to Fe_3O_4 . The wide asymmetric peak at the temperature range of 350–800 °C can be identified as the reduction of Fe_3O_4 to metallic iron [49]. Fig. 5 shows clear shift of the reduction

Table 1Physicochemical properties, apparent activation energy (E_a) and turnover frequency (TOF) of fresh, reduced and used catalysts.

Catalyst	Bulk Composition in weight ratio ^a (%)			$d_{\text{CuO}}/\text{nm}^b$	$d_{\text{Cu}}/\text{nm}^b$		Cu Metal Dispersion ^c	$S_{\text{Cu}}^d/\text{m}^2 \text{ g}^{-1}$
	Cu	Fe	O		Fresh	Reduced		
Pure CuO	87.5	–	12.5	19.9	28.3	28.7	0.1%	0.7
$\text{Cu}_{0.9}\text{Fe}_{0.1}\text{O}_x$	80.0	10.3	9.7	13.2	22.0	27.9	2.2%	16.8
$\text{Cu}_{0.7}\text{Fe}_{0.3}\text{O}_x$	64.2	23.2	12.6	10.1	21.2	26.6	7.7%	26.3
$\text{Cu}_{0.5}\text{Fe}_{0.5}\text{O}_x$	42.1	37.4	20.5	6.7	16.8	19.0	13.5%	29.5
$\text{Cu}_{0.3}\text{Fe}_{0.7}\text{O}_x$	24.6	54.4	21.0	6.6	12.1	16.6	14.8%	32.1
$\text{Cu}_{0.1}\text{Fe}_{0.9}\text{O}_x$	8.6	68.7	22.7	–	16.5	16.6	19.4%	13.6
Pure Fe_2O_3	–	28.5	71.5	–	–	–	–	–
$\text{Cu}_{0.3}\text{Fe}_{0.6}\text{Al}_{0.1}\text{O}_x$	27.3	43.0	21.8	–	9.9	12.3	20.5%	35.9

^a Weight ratio of H_2 -reduced catalysts determined by EDX.^b Determined by the XRD patterns and Scherrer formula.^c Determined by N_2O chemisorption.^d Determined by the calculation of the copper surface area, it is assumed that a reduced copper surface has a surface density of 1.46×10^{19} copper atoms per m^{-2} .

peaks to lower temperature region, compared to that of the pure materials. The peak shoulders of $\text{Cu}-\text{Fe}_3\text{O}_4$ catalysts emerged from lower than 200 °C are designated as the reduction of Fe_2O_3 to Fe_3O_4 . According to former reports [50,51], the introduction of Cu to Fe_2O_3 can shift the reduction temperature of Fe_2O_3 to Fe_3O_4 from 300 °C to 200 °C. We also find that the addition of Fe component can shift the reduction temperature of CuO to metallic Cu lower by as high as 50 °C ($\text{Cu}_{0.3}\text{Fe}_{0.7}\text{O}_x$). This shift proves the enhancement of reducibility after Fe introduction, which is also supported by the XPS analysis. The same conclusion can be made from the CO-TPR results shown in Fig. 5b. However, unlike the reduction in H_2 atmosphere, the reduction of Cu in CO is prior to that of hematite to magnetite. This result agrees to the former report [52], showing the reduction of CuO to metallic Cu^0 in CO is easier than that in H_2 .

3.3. WGS catalytic performances

The WGS catalytic properties of the $\text{Cu}-\text{Fe}_3\text{O}_4$ catalysts are evaluated. The temperature-dependent catalytic activity results are displayed in Fig. 6a. $\text{Cu}_{0.3}\text{Fe}_{0.7}\text{O}_x$ gives the highest CO conversion within the tested temperature range. As can be seen, the activity of $\text{Cu}_{0.9}\text{Fe}_{0.1}\text{O}_x$ is much more improved compared to the one of pure CuO sample, suggesting the pronounced activity promotion by Fe introduction. Pure Fe_3O_4 and $\text{Cu}_{0.1}\text{Fe}_{0.9}\text{O}_x$ show obvious WGS activity only when the temperature is above 300 °C, which suggests that these two Fe-based catalysts are more applicable to HTS process.

The apparent activation energies (E_a) and CO reaction rates (r_{CO}) of WGS over $\text{Cu}-\text{Fe}_3\text{O}_4$ catalysts are shown in Table 3 and Fig. 6b. Different E_a s are obtained from CO consumption rates between 180 °C to 310 °C (Fig. 6c). Among the tested catalysts, $\text{Cu}_{0.1}\text{Fe}_{0.9}\text{O}_x$ gives the E_a of 94.1 kJ mol⁻¹, very similar to that of Fe-Cr catalysts for HTS

(92 kJ mol⁻¹) [2]. Further elevation of Cu content would lead to a substantial decrease in E_a (more than 40 kJ mol⁻¹), suggesting the WGS reaction is promoted and the reaction pathway is changed. As shown in Fig. 6c, the Cu-rich catalysts exhibit similar E_a values, from 45.5 to 51.5 kJ mol⁻¹. Turnover frequencies (TOF) of WGS are determined under differential reaction conditions from the kinetic region. Among the tested catalysts, $\text{Cu}_{0.3}\text{Fe}_{0.7}\text{O}_x$ gives the highest r_{CO} and TOF (0.111 $\text{mmol} \cdot \text{g}^{-1} \cdot \text{s}^{-1}$ and 0.047 s^{-1} at 250 °C).

The data of E_a , r_{CO} and TOF between $\text{Cu}-\text{Fe}_3\text{O}_4$ catalysts and literature reports are listed in Table 3. The r_{CO} of $\text{Cu}-\text{Fe}_3\text{O}_4$ catalyst is transferred into CO conversion per m^{-2} of Cu for comparison. As can be seen, our $\text{Cu}-\text{Fe}_3\text{O}_4$ catalysts exhibit very high WGS activity among the reported Cu-based catalyst, with r_{CO} of 1.46 $\mu\text{mol} \cdot \text{m}^{-2} \cdot \text{s}^{-1}$ $\text{Cu}_{0.3}\text{Fe}_{0.7}\text{O}_x$. However, as also shown in Table 3, the influence of gas composition and reaction temperature should not be neglected, since the introduction of CO_2 and H_2 may significantly alter the reaction equilibrium and CO conversion.

The experimental results of kinetics are further investigated via the effect of reactants (CO and H_2O) partial pressures on the r_{CO} at 300 °C. The apparent reaction orders are also calculated from the r_{CO} data. Fig. 6d shows WGS reaction orders in CO and H_2O with varying partial pressures of the reactants. The apparent reaction orders in H_2O for $\text{Cu}_{0.1}\text{Fe}_{0.9}\text{O}_x$, $\text{Cu}_{0.3}\text{Fe}_{0.7}\text{O}_x$ and $\text{Cu}_{0.7}\text{Fe}_{0.3}\text{O}_x$ are 0.06, 0.23 and 0.34, respectively. These low H_2O orders suggest that the hydroxyl group on the catalyst surface is saturated during WGS reaction. The reaction order in CO for $\text{Cu}_{0.3}\text{Fe}_{0.7}\text{O}_x$ (0.99) is close to that of $\text{Cu}_{0.7}\text{Fe}_{0.3}\text{O}_x$ (0.95), indicating similar weak CO adsorption. However, the CO reaction order for $\text{Cu}_{0.1}\text{Fe}_{0.9}\text{O}_x$ is obviously lower (0.42), which demonstrates strong CO adsorption on the catalyst surface.

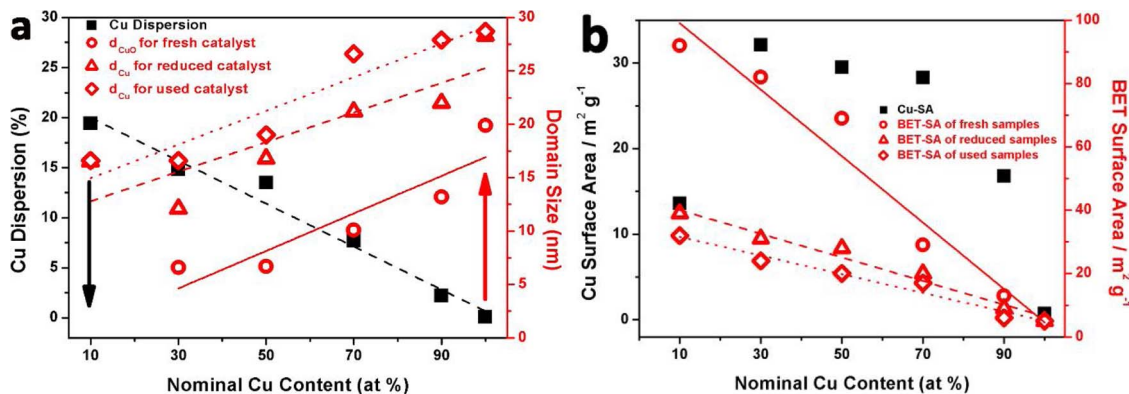


Fig. 2. (a) Cu dispersion/crystallite sizes of CuO and Cu as a function of Cu content; (b) Cu surface area and BET surface area as a function of Cu content.

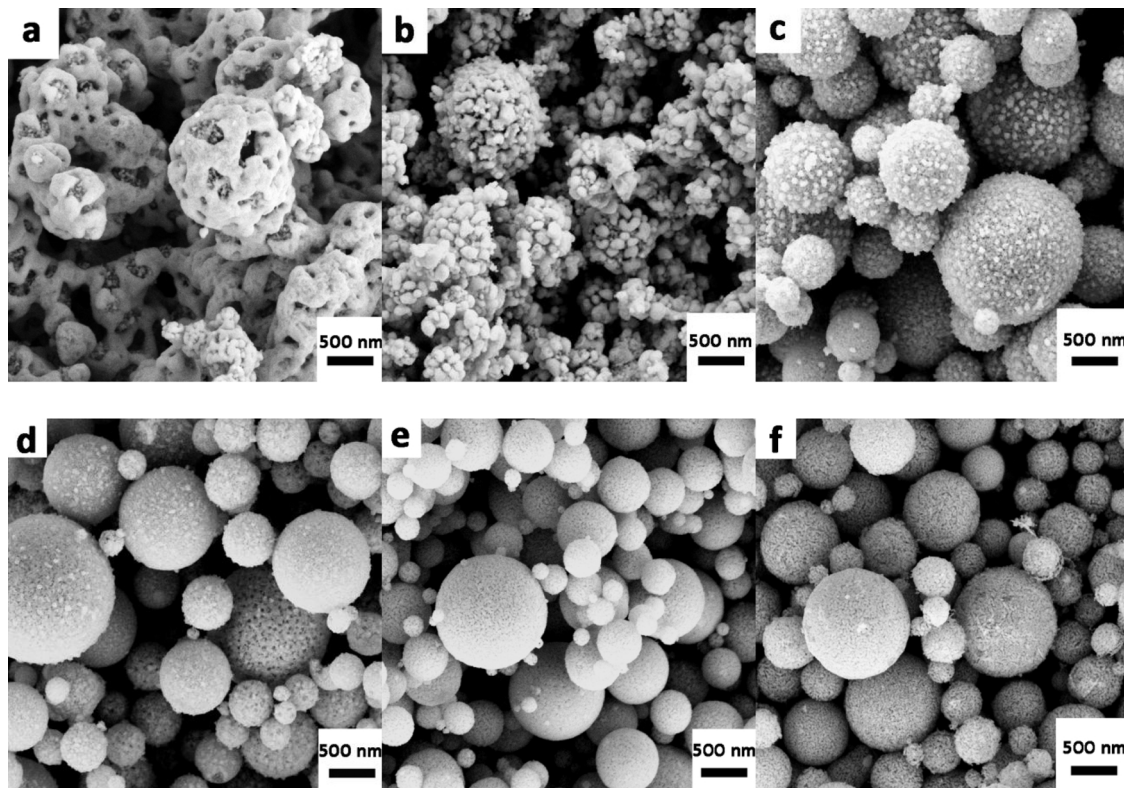


Fig. 3. SEM images of representative catalysts after H_2 reduction treatment: (a) $\text{Cu}_{0.9}\text{Fe}_{0.1}\text{O}_x$; (b) $\text{Cu}_{0.7}\text{Fe}_{0.3}\text{O}_x$; (c) $\text{Cu}_{0.5}\text{Fe}_{0.5}\text{O}_x$; (d) $\text{Cu}_{0.3}\text{Fe}_{0.7}\text{O}_x$; (e) $\text{Cu}_{0.1}\text{Fe}_{0.9}\text{O}_x$; (f) pure Fe_3O_4 .

3.4. In-situ DRIFTS studies

The reaction process and adsorption of reactants over Cu- Fe_3O_4 catalysts are investigated using *in-situ* DRIFTS. Fig. 7a displays the DRIFTS data of CO and H_2O adsorbed on the previously reduced Cu- Fe_3O_4 samples at 200 °C under steady state. According to former reports [32,35], the bands at around 2110 and 2173 cm^{-1} assign to adsorbed and gas phased CO on the catalysts surface, respectively. The CO adsorption on Cu-species seems to show up as $\text{Cu}^+ \text{-CO}$ rather than $\text{Cu}^0 \text{-CO}$, while $\text{Cu}^0 \text{-CO}$ species can absorb at the similar frequency as $\text{Cu}^+ \text{-CO}$ species when Cu dispersion is high [53]. The weakly adsorbed CO_2 gives a doublet at 2327 and 2360 cm^{-1} . The broad peak located between 3000–3600 cm^{-1} , which is observed for samples with high Fe content, is characteristic of OH stretching of the adsorbed water [54]. As shown in Fig. 7b, the $\text{Cu}_{0.3}\text{Fe}_{0.7}\text{O}_x$ catalyst exhibits strong intensity of CO adsorption. The formation of CO_2 from the start indicates the

Table 2

Binding energies of core electrons and XPS atomic ratios of the fresh Cu- Fe_3O_4 catalysts.

Catalyst	XPS Binding Energies (eV)		Surface Elemental Ratio ^a (%)	
	Cu 2p _{2/3}	Fe 2p _{2/3}	Cu/(Cu + Fe)	Fe/(Cu + Fe)
Pure CuO	933.6	—	—	—
$\text{Cu}_{0.9}\text{Fe}_{0.1}\text{O}_x$	933.5	711.2	90.04(86.80)	9.96(13.20)
$\text{Cu}_{0.7}\text{Fe}_{0.3}\text{O}_x$	933.0	711.1	71.10 (69.84)	28.90 (30.16)
$\text{Cu}_{0.5}\text{Fe}_{0.5}\text{O}_x$	932.8	711.1	56.33 (55.16)	43.67 (44.84)
$\text{Cu}_{0.3}\text{Fe}_{0.7}\text{O}_x$	932.4	711.0	41.86 (40.97)	58.14 (59.03)
$\text{Cu}_{0.1}\text{Fe}_{0.9}\text{O}_x$	932.2	710.8	19.58 (13.54)	80.42 (86.46)
Pure Fe_2O_3	—	710.6	—	—

^a Values in parenthesis are elemental ratio determined by EDX.

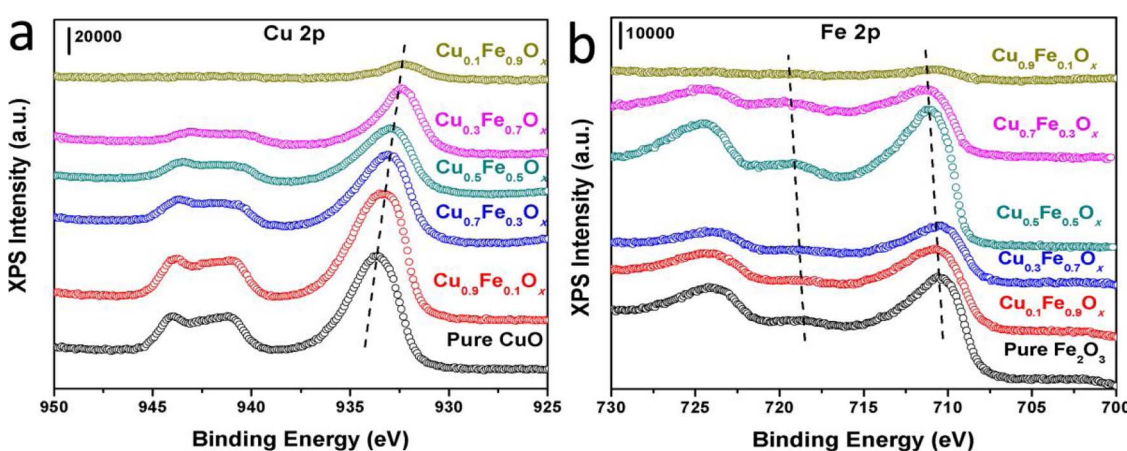
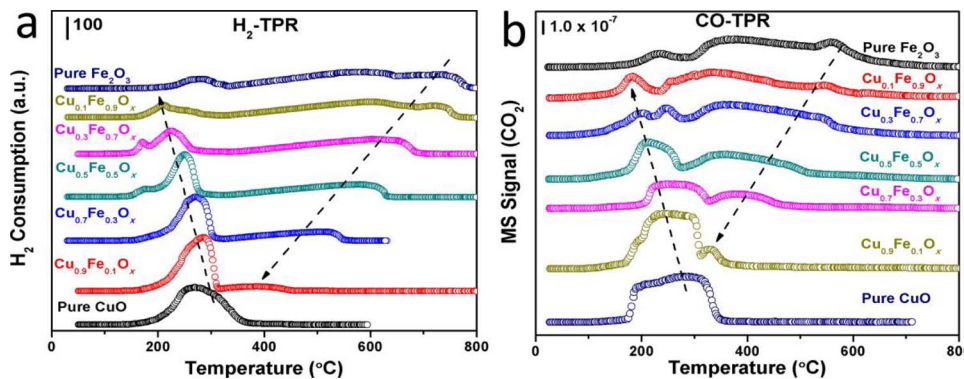


Fig. 4. X-ray photoelectron spectroscopy (XPS) spectra of the Cu- Fe_3O_4 catalysts: (a) Cu 2p and (b) Fe 2p spectra for the fresh samples.



WGS reaction is undergoing. After 30 min of reaction, the adsorbed CO peak gradually fades while the increase in intensity of CO_2 doublet is much more pronounced, indicating the conversion of CO to CO_2 due to the undergoing WGS reaction. In comparison, although strong CO adsorption is observed for $\text{Cu}_{0.1}\text{Fe}_{0.9}\text{O}$ in Fig. 7c, the adsorbed CO does not convert into CO_2 in the tested 30 min.

Two models of mechanism are well known for explaining WGS reaction over different catalysts, namely, the associative and redox mechanisms [55,56], have been widely debated. In Fig. 7, the adsorption profiles show no observable bands in the region of $2800\text{--}3000\text{ cm}^{-1}$, where typical C–H stretching [31] for formate species takes place. This observation suggests that the formate intermediate for associative mechanism is not present in our study. Thus, coupled with former reports [31,35], we conclude that the $\text{Cu}-\text{Fe}_3\text{O}_4$ WGS catalysts follow the

operative mechanism of redox pathway rather than the associative one.

The CO sorption DRIFTS measurement is carried out to examine the ability of CO sorption for $\text{Cu}_{0.3}\text{Fe}_{0.7}\text{O}_x$ and $\text{Cu}_{0.1}\text{Fe}_{0.9}\text{O}_x$. As shown in Fig. 8a and c, both catalysts exhibit strong intensity of CO adsorption. However, the CO desorption for $\text{Cu}_{0.3}\text{Fe}_{0.7}\text{O}_x$ is easily completed by N_2 sweep (Fig. 8b), while the CO adsorption for $\text{Cu}_{0.1}\text{Fe}_{0.9}\text{O}_x$ remains strong after 30 min (Fig. 8d). These results corresponds well to our apparent CO reaction orders measurements in Fig. 6d.

3.5. TPD measurements

The adsorption properties of CO_2 can make a great impact on the WGS catalytic performance. Fig. S4 displays the CO_2 -TPD profiles of reduced $\text{Cu}-\text{Fe}_3\text{O}_4$ catalysts. Two typical desorption peaks emerge for

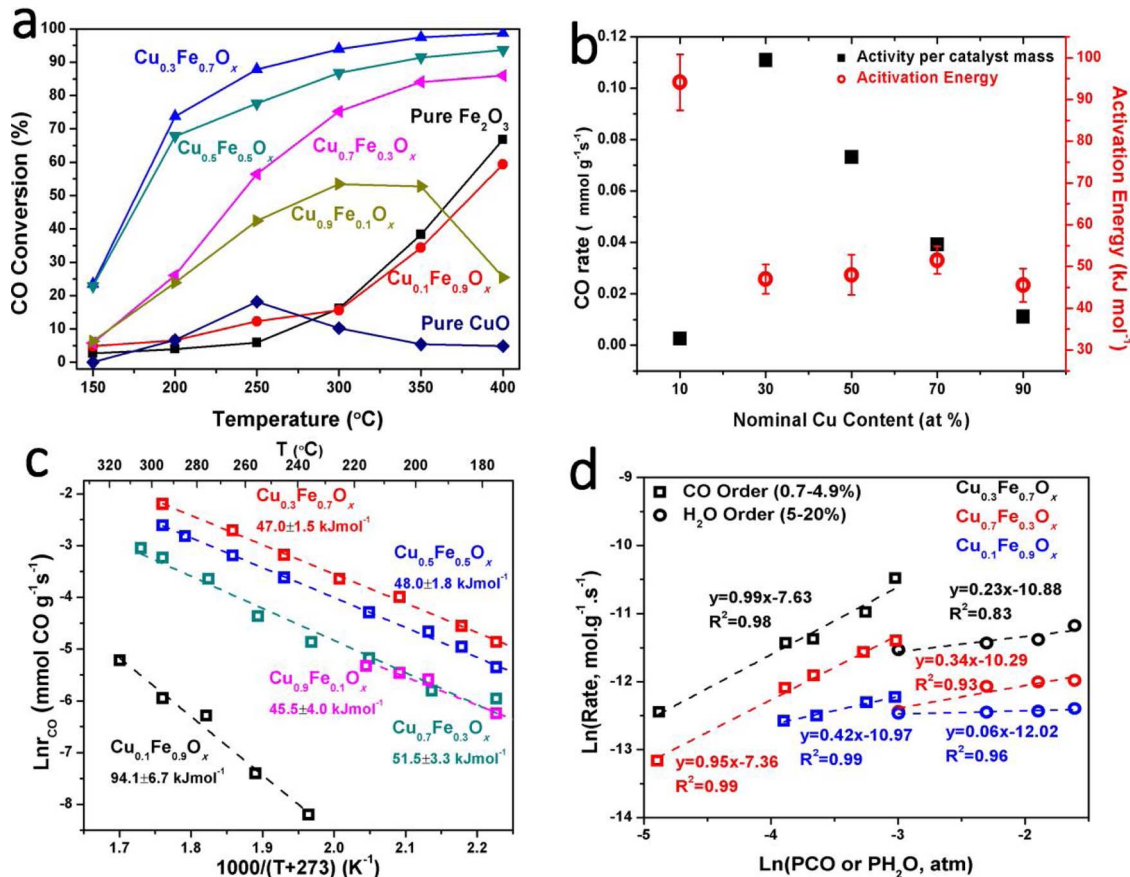


Fig. 6. (a) Temperature-dependent CO conversion of WGS reaction on $\text{Cu}-\text{Fe}_3\text{O}_4$ catalysts (100 mg of catalysts, 1 atm total pressure, 2.2% CO, 15% H_2O and the rest of N_2 , GHSV = 42,000 $\text{cm}^3\text{ min}^{-1}\text{ g}^{-1}$); (b) Apparent activation energies (E_a) and CO reaction rates (r_{CO}) as a function of Cu content (250 °C, 20 mg of catalysts, 1 atm total pressure, 2.2% CO, 15% H_2O and the rest of N_2); (c) Arrhenius plots of CO reaction rate (r_{CO}) obtained over $\text{Cu}-\text{Fe}_3\text{O}_4$ catalysts (20 mg of catalysts, 1 atm total pressure, 2.2% CO, 15% H_2O and the rest of N_2); (d) Power law with the effects of CO and H_2O on r_{CO} over $\text{Cu}-\text{Fe}_3\text{O}_4$ catalysts (300 °C, 0.7–4.9% CO, 5–20% H_2O , balance N_2).

Table 3Comparisons of water gas shift activity results of Cu-Fe₃O₄ catalysts with conventional catalysts and other reported findings.

Catalyst	Conditions	T/°C	E _a /kJ mol ⁻¹	Rate/10 ⁻⁶ mol m ⁻² s ⁻¹	TOF/s ⁻¹	Reference
Cu _{0.3} Fe _{0.7} O _x	2.2%CO, 15%H ₂ O, balance N ₂	250	47.0	1.46	0.047	This work
Cu _{0.3} Fe _{0.6} Al _{0.1} O _x	2.2%CO, 15%H ₂ O, balance N ₂	250	44.9	3.98	0.136	This work
Cu/ZnO/La	7%CO, 23%H ₂ O, 8.5% CO ₂ , 37.5% H ₂ , balance N ₂	230	31.6 – 43.1	–	0.004 – 0.018	[7]
5at.%Ni-Ce(10%La)O _x	1%CO, 2%H ₂ O, balance N ₂	275 – 300	38.2	–	–	[8]
5at.%Cu-Ce(10%La)O _x	1%CO, 2%H ₂ O, balance N ₂	175 – 300	19.2 – 30.4	–	–	[8]
CuO/ZnO/Al ₂ O ₃	7%CO, 22%H ₂ O, 8.5% CO ₂ , 37% H ₂ , balance Ar	180 – 200	86	0.91	–	[9]
Cu (111)	1%CO, 2.6%H ₂ O, balance N ₂	340	71	0.32	–	[10]
Cu (110)	1%CO, 2.6%H ₂ O, balance N ₂	340	42	14	–	[11]
5Ni5Cu/CeO ₂	7%CO, 22%H ₂ O, 10% CO ₂ , 20% H ₂ , balance He	350	41.3	0.33	0.013	[19]
10Cu/CeO ₂	7%CO, 22%H ₂ O, 10% CO ₂ , 20% H ₂ , balance He	350	57.6	0.15	0.013	[19]

all tested samples [27,29,31]: First one centered at 100–130 °C (peak α), denoted as weak basic site and the other one centered at 330–350 °C (peak β), denoted as strong basic site. The intensity of peak α for pure CuO sample is very low and it is strongly enhanced after Fe addition. Peak β is absent for pure CuO sample and is pronounced for samples with high Fe content. Among all the catalysts, Cu_{0.3}Fe_{0.7}O_x gives the strongest intensities of both peaks. These observations indicate that the interaction between metallic Cu⁰ and Fe₃O₄ remarkably facilitates the CO₂ adsorption on the Cu-Fe₃O₄ catalysts.

3.6. In-situ XRD measurements

The structural transformation of the Cu-Fe₃O₄ catalysts is investigated using *in-situ* XRD. Cu_{0.3}Fe_{0.7}O_x and Cu_{0.7}Fe_{0.3}O_x are chosen for comparisons, and Fig. 9 illustrates the relative *in-situ* XRD patterns. Both catalysts go through H₂ reduction prior to the test in a 2% CO/Ar

gas mixture. As shown in Fig. 9a, after H₂ reduction, the characteristic peaks of Cu₂O and CuO are present for Cu_{0.7}Fe_{0.3}O_x and no peaks of metallic Cu⁰ are observed. In CO/Ar atmosphere, with increasing reduction temperature, characteristic peaks of CuO and Cu₂O gradually diminish and finally vanish at 250 °C. Meanwhile, peaks of metallic Cu⁰ emerge at 200 °C and sharpen. These results indicate that the CuO component in Cu_{0.7}Fe_{0.3}O_x is reduced incompletely by H₂ and the following reduction in CO/Ar atmosphere possesses two steps, CuO to Cu₂O then further to metallic Cu⁰. The Fe₃O₄ characteristic peaks for Cu_{0.7}Fe_{0.3}O_x, which are partially overlapped with those of CuO, also diminish with temperature increasing and a shoulder peak ascribed to metallic Fe⁰ emerges at 350 °C. For Cu_{0.3}Fe_{0.7}O_x (Fig. 9b), CuO is totally reduced to metallic Cu⁰ by H₂ as no peaks of CuO or Cu₂O are observed after H₂ reduction. The intensity of Cu⁰ characteristic peaks remains low within the tested temperature range. The Fe₃O₄ reduction of Cu_{0.3}Fe_{0.7}O_x is similar to that of Cu_{0.7}Fe_{0.3}O_x, which exhibits decreasing

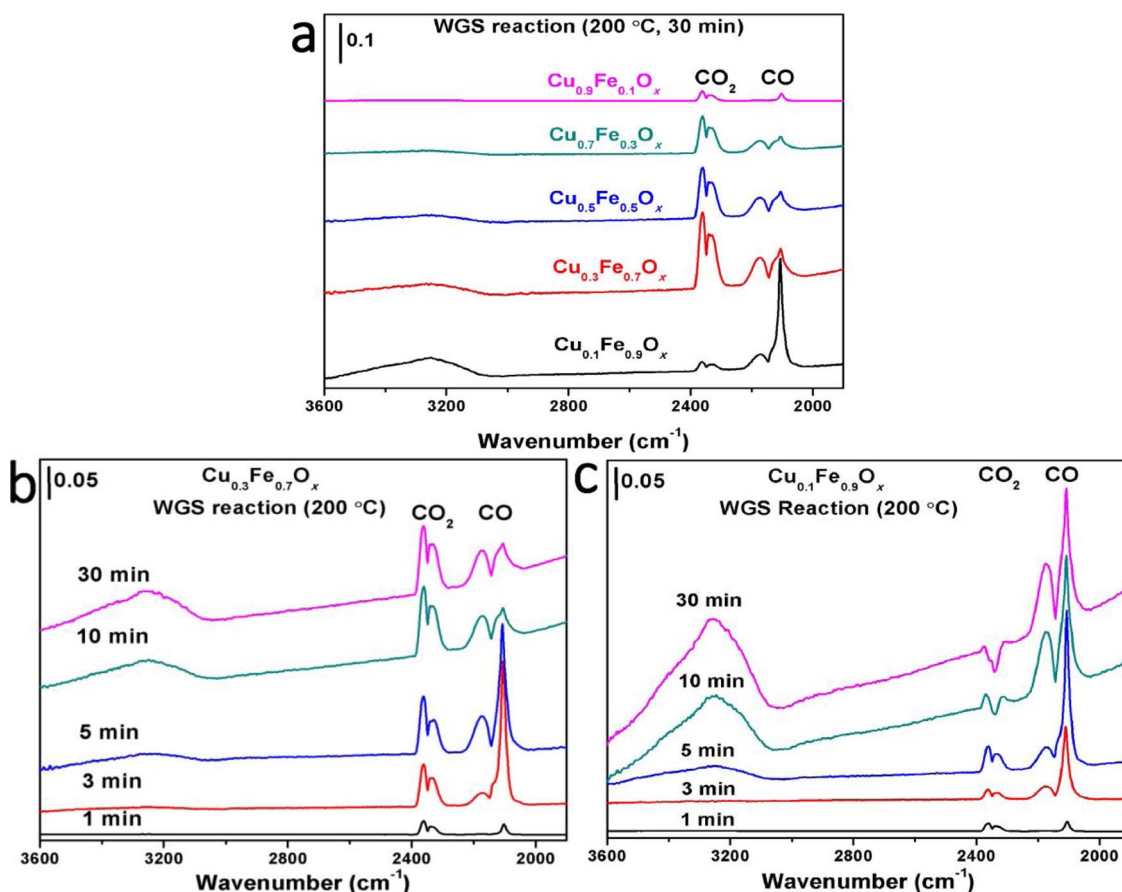


Fig. 7. (a) *In-situ* diffuse reflectance infrared Fourier transform spectroscopy (DRIFTS) results of WGS measurement on reduced Cu-Fe₃O₄ catalysts; (b, c) Time-dependent *in-situ* DRIFTS results of reduced Cu_{0.3}Fe_{0.7}O_x and Cu_{0.1}Fe_{0.9}O_x.

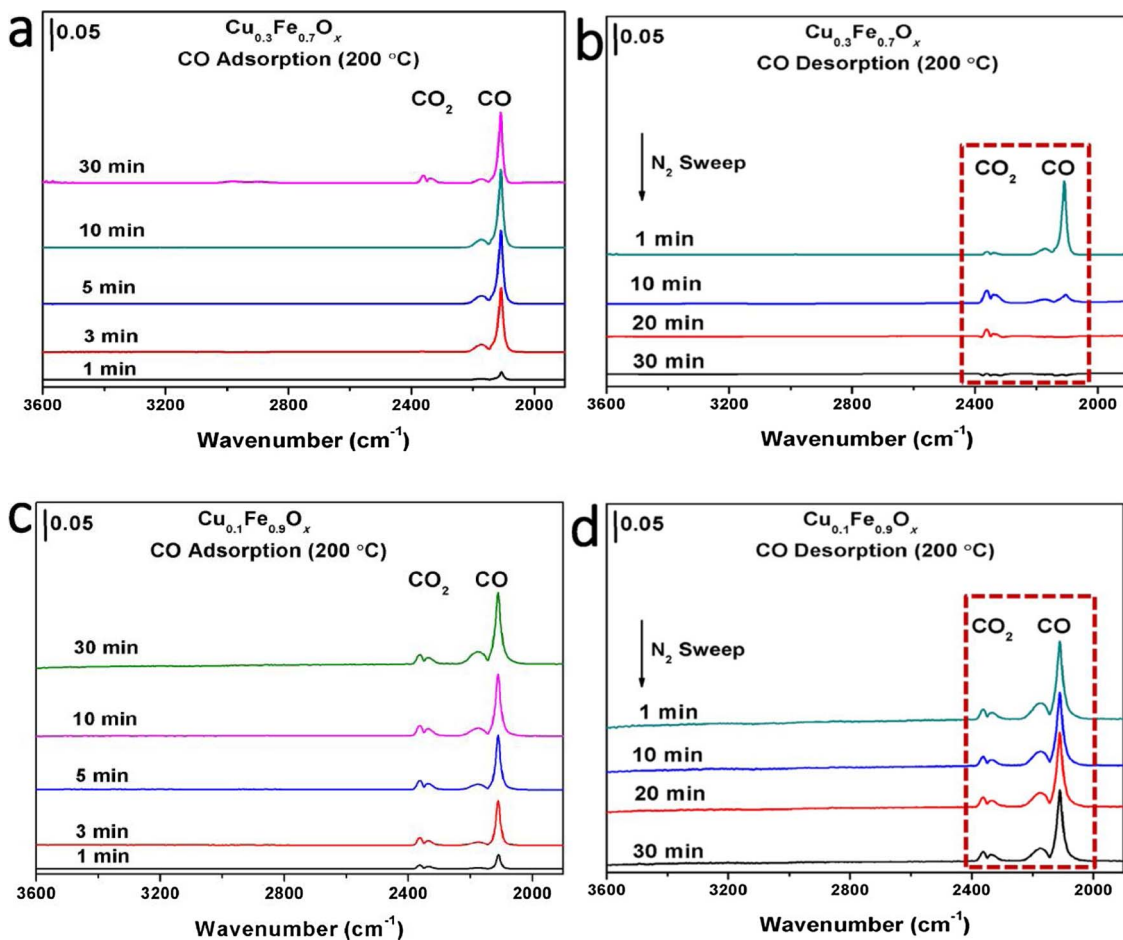


Fig. 8. CO adsorption-desorption DRIFTS profiles of reduced (a, b) $\text{Cu}_{0.3}\text{Fe}_{0.7}\text{O}_x$ and (c, d) $\text{Cu}_{0.1}\text{Fe}_{0.9}\text{O}_x$.

intensities of magnetite characteristic peaks and appearance of Fe^0 peak with increasing temperature.

3.7. WGS stability tests

The catalytic stabilities for WGS of $\text{Cu}_{0.7}\text{Fe}_{0.3}\text{O}_x$ and $\text{Cu}_{0.3}\text{Fe}_{0.7}\text{O}_x$ are studied via time-on-stream-dependent tests at 250 °C. Fig. S5a presents the results of long-term stability tests, showing that both $\text{Cu}-\text{Fe}_3\text{O}_4$ catalysts go through consistent deactivation under WGS conditions. The CO conversion of $\text{Cu}_{0.7}\text{Fe}_{0.3}\text{O}_x$ decreases from 66% to 15% within 140 h, and that of $\text{Cu}_{0.3}\text{Fe}_{0.7}\text{O}_x$ decreases from 80% to 40%. Former

report has found that the addition of Fe promoter can improve the WGS stability for supported Cu/SiO_2 catalysts [31]. However, for the bulk $\text{Cu}-\text{Fe}_3\text{O}_4$ catalysts prepared via ASSA, although the Cu-Fe interaction has been proved, the catalytic performance is not stable under test conditions. Such a phenomenon can result from sintering, which may destruct the structure of the surface Cu sites. Here, enlightened by the creation of traditional Cu-Zn-Al catalyst, we introduce Al component as partial replacement of Fe for $\text{Cu}_{0.3}\text{Fe}_{0.7}\text{O}_x$, aiming to develop a more stable LTS catalyst. As shown in Fig. S5, a nominal 10 at% replacement of Fe to Al slightly boosts the WGS activity, and further addition of Al causes the decline of CO conversion. The r_{CO} and TOF of

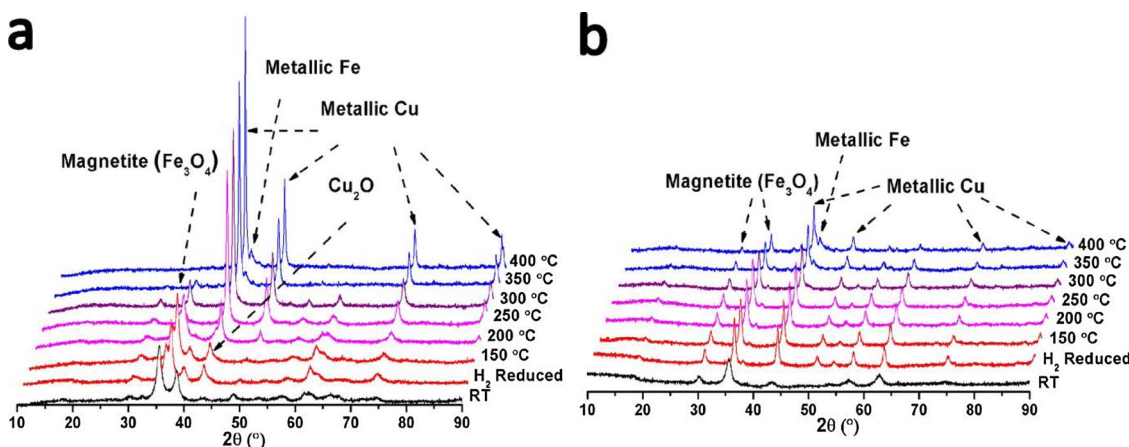
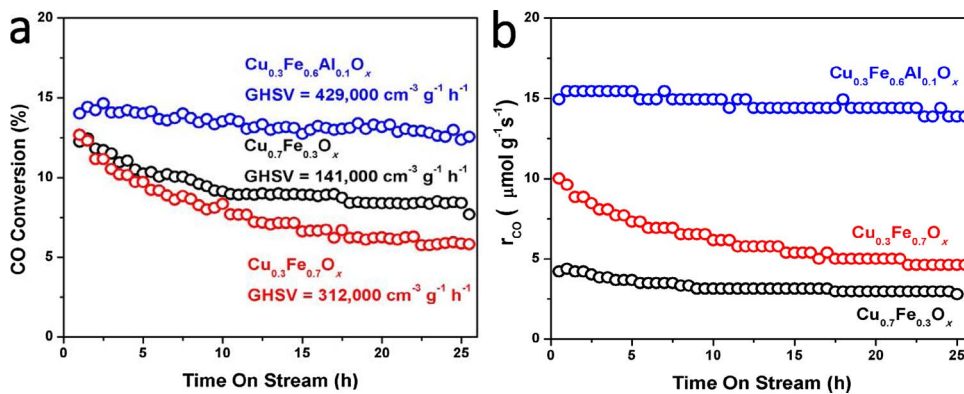


Fig. 9. In-situ X-ray diffraction (in-situ XRD) patterns of (a) $\text{Cu}_{0.7}\text{Fe}_{0.3}\text{O}_x$ and (b) $\text{Cu}_{0.3}\text{Fe}_{0.7}\text{O}_x$ in 2%CO/Ar gas under different temperature after H_2 reduction at 300 °C for 0.5 h.



$\text{Cu}_{0.3}\text{Fe}_{0.6}\text{Al}_{0.1}\text{O}_x$ are also boosted compared to those of $\text{Cu}_{0.3}\text{Fe}_{0.7}\text{O}_x$ (Table 3). The increase in activity may arise from the enhanced Cu dispersion of $\text{Cu}_{0.3}\text{Fe}_{0.6}\text{Al}_{0.1}\text{O}_x$, as shown in Table 1. During 150 h of test (Fig. S5a), the CO conversion of WGS reaction on $\text{Cu}_{0.3}\text{Fe}_{0.6}\text{Al}_{0.1}\text{O}_x$ is finally held above 85%, showing greatly improved stability compared to $\text{Cu}_{0.3}\text{Fe}_{0.7}\text{O}_x$.

In order to exclude the influence of mass transport, stability tests are also carried out in the kinetic region. As illustrated in Fig. 10a, the WGS conversion $\text{Cu}_{0.3}\text{Fe}_{0.7}\text{O}_x$ and $\text{Cu}_{0.7}\text{Fe}_{0.3}\text{O}_x$ both drop down during the stability tests. The deactivation for $\text{Cu}_{0.3}\text{Fe}_{0.7}\text{O}_x$ is more severe because of the higher space velocity. Fig. 10b gives the stability of r_{CO} in the kinetic region. As can be seen, the low space velocity results in the low r_{CO} of $\text{Cu}_{0.7}\text{Fe}_{0.3}\text{O}_x$. $\text{Cu}_{0.3}\text{Fe}_{0.7}\text{O}_x$ exhibits unstable nature under high space velocity while the stability of $\text{Cu}_{0.3}\text{Fe}_{0.6}\text{Al}_{0.1}\text{O}_x$ is well maintained. According to the TEM images shown in Fig. S6, after long-term stability test, the spherical morphology of $\text{Cu}_{0.3}\text{Fe}_{0.6}\text{Al}_{0.1}\text{O}_x$ is well preserved, and no obvious sintering happens after the long-term stability test with Al introduction.

4. Discussion

4.1. Redox properties and structure of $\text{Cu}-\text{Fe}_3\text{O}_4$ catalysts

The superiority of ASSA over traditional preparation method for bulk catalysts, such as co-precipitation method, lies in the pronounced compositional interaction and higher specific surface area, which has been proved before [43]. However, in this work, Fig. 2b demonstrates that the high specific surface area seems not to benefit WGS activity, since all catalysts possess low BET surface area after reaction. This deduction agrees with Yahiro's work [26], showing BET surface area gives limited impact on WGS activity for Cu catalysts. Meanwhile, Table 1 shows that the Fe introduction creates highly dispersed Cu species. The Cu surface area determined by the dispersion is proportional to the WGS activity (Figs. 2b and 6b).

Both the *ex-situ* and *in-situ* XRD measurements (Figs. 1 and 9) prove that the addition of Fe helps to reduce and maintain the crystalline size of Cu^0 (Fig. 2a). Therefore, the Fe component crystallizes as the skeleton of the $\text{Cu}-\text{Fe}_3\text{O}_4$ microspheres, which enhances the Cu surface area by improving dispersion of Cu due to the Cu-Fe interaction. It is worth noticing that the high Cu dispersion and the large Cu^0 size seem contradictory. This mismatch may result from the low sensitivity of XRD to nanoparticles, which will be further discussed later. When Fe component is introduced, the TPR peaks of copper oxide shift to lower temperature (Fig. 5). This shift corresponds well to the XPS analysis (Fig. 4), which suggests an increase of Cu core electron density with increasing Fe addition.

Since metallic Cu^0 is easily oxidized in the air, it is difficult to determine whether it is Cu^0 or Cu^+ serves as the active phase *via ex-situ* XRD or XPS. Herein, we performed temperature-programmed surface reaction (TPSR), followed by H_2 -TPR, to examine the possible existence

of Cu^+ during the WGS reaction. As shown in Fig. 11a, the WGS reaction starts to take place from 150 °C. CO_2 and H_2 formation is ongoing throughout the testing temperature range. Fig. 11b illustrates that TPR profile for $\text{Cu}_{0.3}\text{Fe}_{0.7}\text{O}_x$ after TPSR gives no reduction peaks, suggesting all Cu-species remain metallic state during the reaction. Thus, it has been proved that the active phase of $\text{Cu}-\text{Fe}_3\text{O}_4$ catalysts for WGS reaction is metallic Cu^0 .

4.2. Adsorption/Desorption behavior of $\text{Cu}-\text{Fe}_3\text{O}_4$ catalysts – the impact of Fe

The *in-situ* DRIFTS results in Fig. 7a have shown that $\text{Cu}_{0.1}\text{Fe}_{0.9}\text{O}_x$ possesses the strongest CO adsorption among all the $\text{Cu}-\text{Fe}_3\text{O}_4$ catalysts, but its weak signal of CO_2 suggests low WGS activity (Fig. 7c). In comparison, the CO_2 from WGS reaction is clearly observed for $\text{Cu}_{0.3}\text{Fe}_{0.7}\text{O}_x$ (Fig. 7b). The reason may lie in the over strong CO adsorption for $\text{Cu}_{0.1}\text{Fe}_{0.9}\text{O}_x$, leading to the self-poisoning from CO coverage. This deduction is evidenced by the CO sorption DRIFTS profiles shown in Fig. 8. Though strong CO adsorption is observed on both $\text{Cu}_{0.3}\text{Fe}_{0.7}\text{O}_x$ and $\text{Cu}_{0.1}\text{Fe}_{0.9}\text{O}_x$ (Fig. 8a and c), the CO desorption in N_2 shows different results. The adsorbed CO on $\text{Cu}_{0.3}\text{Fe}_{0.7}\text{O}_x$ can be easily swept by N_2 (Fig. 8b). As for $\text{Cu}_{0.1}\text{Fe}_{0.9}\text{O}_x$, the CO adsorption is so strong that N_2 sweep cannot desorb CO from the surface (Fig. 8d). Fig. S7 also illustrates the CO sorption results of $\text{Cu}_{0.7}\text{Fe}_{0.3}\text{O}_x$, showing weak CO adsorption and quick CO desorption. The difference in CO adsorption abilities corresponds well to the different CO reaction orders of the catalysts (shown in Fig. 6d), suggesting strong CO adsorption for $\text{Cu}_{0.1}\text{Fe}_{0.9}\text{O}_x$ and weak adsorption for $\text{Cu}_{0.7}\text{Fe}_{0.3}\text{O}_x$ [19].

In Fig. 7, both $\text{Cu}_{0.3}\text{Fe}_{0.7}\text{O}_x$ and $\text{Cu}_{0.1}\text{Fe}_{0.9}\text{O}_x$ exhibit strong intensity of CO adsorption. In line with the Cu dispersion results in Table 1, it is reasonable that the highly dispersed Cu^0 is the adsorption site for CO, since $\text{Cu}_{0.3}\text{Fe}_{0.7}\text{O}_x$ and $\text{Cu}_{0.1}\text{Fe}_{0.9}\text{O}_x$ possess superior reducibility and Cu dispersion. Moreover, in Fig. 7a, the intensity increase of the OH stretching peak ($3000\text{--}3600 \text{ cm}^{-1}$) for greater Fe-containing catalysts demonstrates that the addition of Fe_3O_4 can improve the water adsorption. Based on these observations, we believe that the enhanced adsorption of both WGS reactants (CO and H_2O) after Fe introduction facilitates the conduction of WGS reaction, resulting in $\text{Cu}_{0.3}\text{Fe}_{0.7}\text{O}_x$ giving the best WGS performance among all the $\text{Cu}-\text{Fe}_3\text{O}_4$ catalysts. At the same time, the CO adsorption on $\text{Cu}_{0.1}\text{Fe}_{0.9}\text{O}_x$ is too strong to fulfill the reaction, as demonstrated by the CO reaction order and DRIFTS results in Fig. 6d and 8.

Former reports have emphasized the importance of basicity for WGS catalysts [27,29,31], which lies in the stabilization of formate intermediates assuming the associative mechanism. The reports of Trillo et al. [57] and Ai [58] claim that the formic acid intermediate is decomposed to CO_2 and H_2 over basic metal oxides, while to CO and H_2O over acid oxides. However, the *in-situ* DRIFTS results (Fig. 7) have proved that WGS reaction over the $\text{Cu}-\text{Fe}_3\text{O}_4$ catalysts follows the redox mechanism, so the presumption that the catalysts basicity is important

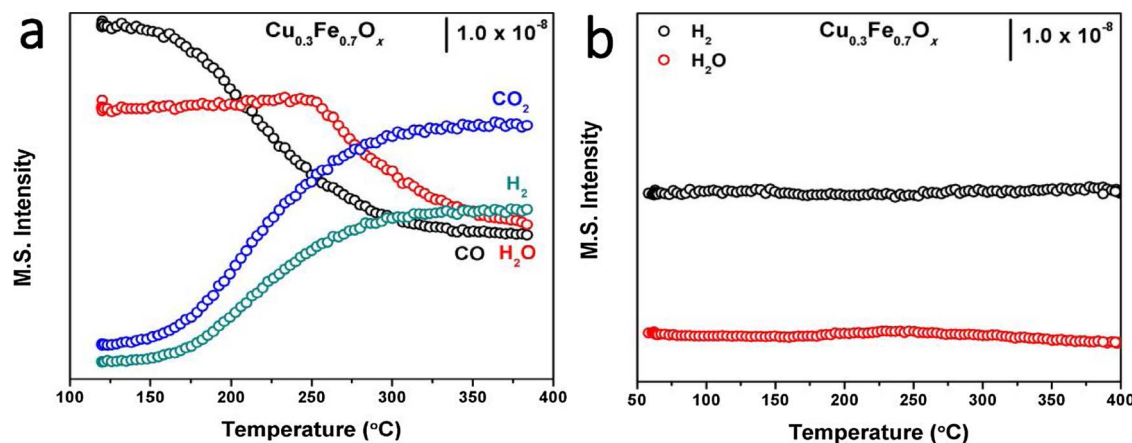


Fig. 11. Temperature-programmed surface reaction (TPSR) results of $\text{Cu}_{0.3}\text{Fe}_{0.7}\text{O}_x$; (b) H_2 -TPR profiles after TPSR of $\text{Cu}_{0.3}\text{Fe}_{0.7}\text{O}_x$. (200 mg of catalysts, 1 atm total pressure, 2% CO, 2% H_2O and the rest of N_2 , total flow = $30 \text{ cm}^3 \text{ min}^{-1}$).

via stabilizing formate intermediates does not make sense in the $\text{Cu}-\text{Fe}_3\text{O}_4$ system here. However, it is noteworthy that the adsorption of CO_2 for $\text{Cu}_{0.3}\text{Fe}_{0.7}\text{O}_x$ is higher than that of the reduced pure Fe_3O_4 sample (Fig. S4). Therefore, the enhanced CO_2 adsorption of the $\text{Cu}-\text{Fe}_3\text{O}_4$ catalysts is not due to the increasing amount of Fe component, indicating Fe_3O_4 is not serving as the absorbing site for CO_2 . The enhanced CO_2 adsorption may result from the increased $\text{Cu}-\text{Fe}_3\text{O}_4$ interface, which has been characterized and stressed great importance in promoting WGS reaction by Tao et al. [59].

4.3. WGS activity, stability and deactivation-Optimization of Cu content

The enhancement of reducibility and dispersion of Cu species by Fe introduction has been demonstrated by the TPR and XPS analyses. This enhancement agrees well with the activity results in Fig. 6a, which illustrates an increasing activity for catalysts with more Fe content until 70%. Besides, Fig. 6a also reflects information of the active phase. The pure CuO sample gives very low Cu dispersion (Table 1) and CO conversion (Fig. 6a). Its *in-situ* DRIFTS results (Fig. S8) also show very weak CO adsorption. Given the Cu component is responsible for CO adsorption and WGS activity in $\text{Cu}-\text{Fe}_3\text{O}_4$ catalysts, it is clear that highly dispersed Cu^0 is the more active phase rather than the bulk one. According to Fig. 6a, $\text{Cu}_{0.9}\text{Fe}_{0.1}\text{O}_x$ gives much improved activity than pure CuO, and the boost of activity is maintained when Fe addition is down to 5 at% (Fig. S9). Thus, we can conclude that in our $\text{Cu}-\text{Fe}_3\text{O}_4$ system, the presence of Fe_3O_4 created large amount of highly dispersed Cu^0 , and this highly dispersed Cu^0 with superior reducibility serves as more active phase for WGS rather than the bulk ones.

The high Cu dispersion of $\text{Cu}-\text{Fe}_3\text{O}_4$ catalysts is to be studied on a profounder level. According to Table 1, the d_{Cu} and Cu dispersion of $\text{Cu}_{0.3}\text{Fe}_{0.7}\text{O}_x$ are 16.6 nm and 14.8%, respectively. Assuming that all Cu^0 exists as 15 nm spherical particles, the Cu dispersion is around 9.1% [60], and this is much lower than the tested data. We reckon that there are some smaller Cu^0 species those are left out. TEM images can give straight evidence of size and morphology. As shown in Fig. S10a, the $\text{Cu}_{0.3}\text{Fe}_{0.7}\text{O}_x$ microsphere exhibits interior-hollow structure after H_2 reduction. Magnification of the hollow part shows no large particles (more than 15 nm), indicating the existence of small Cu species in the catalyst. Interestingly, in the crushed pieces of $\text{Cu}_{0.3}\text{Fe}_{0.7}\text{O}_x$ (exhibited in Fig. S10b), many small particles (less than 10 nm) can be observed. The interplanar d -spacing is 0.203 nm, very close to 0.208 nm of Cu (111). Thus, the high Cu dispersion can be explained since smaller Cu species are observed. After H_2 reduction, some of the Cu^0 maintained small size (less than 10 nm), while the others aggregated to form large particles (more than 15 nm).

The elimination of WGS activity *via* sintering is typical for

traditional Cu-Zn catalysts [61–63]. Based on the observations of morphology change in Fig. 3 and S6, it is very likely that the deactivation (Fig. 10 and S5) of the catalysts arises from sintering. In addition, the high Cu-containing catalysts in Fig. S9 go through deactivation at 400 °C, which indicates that too much of Cu content are not preserved under high temperature and reductive atmosphere. XRD patterns in Fig. S11 further evidence that the sintering for $\text{Cu}_{0.7}\text{Fe}_{0.3}\text{O}_x$ and $\text{Cu}_{0.3}\text{Fe}_{0.7}\text{O}_x$ takes place.

In Fig. 12, the variation of WGS activity with tuning Cu content exhibits a volcano curve. $\text{Cu}_{0.3}\text{Fe}_{0.7}\text{O}_x$ possesses the peak WGS activity. The WGS activity is proportional to the Cu surface area. Based on the above findings, the volcano curve can be explained by the compromise of state and amount of Cu. As shown in Fig. 12, the addition of Fe component improves the Cu dispersion, and in turn increases the Cu surface area. When the Cu proportion is higher than that of $\text{Cu}_{0.3}\text{Fe}_{0.7}\text{O}_x$, excessive amount of Cu sinters and leads to serious deactivation (Fig. 3a and b, Fig. 10). When the Cu proportion is lower than that of $\text{Cu}_{0.3}\text{Fe}_{0.7}\text{O}_x$, the samples suffer from CO poisoning (Fig. 8d) and insufficient Cu content. Thus, the optimization through balancing Cu content is crucial for controlling the WGS activity on $\text{Cu}-\text{Fe}_3\text{O}_4$ bulk catalysts, and it results in that $\text{Cu}_{0.3}\text{Fe}_{0.7}\text{O}_x$ reveals the best catalytic performance. The tri-component $\text{Cu}-\text{Fe}_3\text{O}_4-\text{Al}_2\text{O}_3$ catalyst shows outstanding WGS activity and stability, probably due to the improved Cu surface area (Table 1) and enhanced interaction.

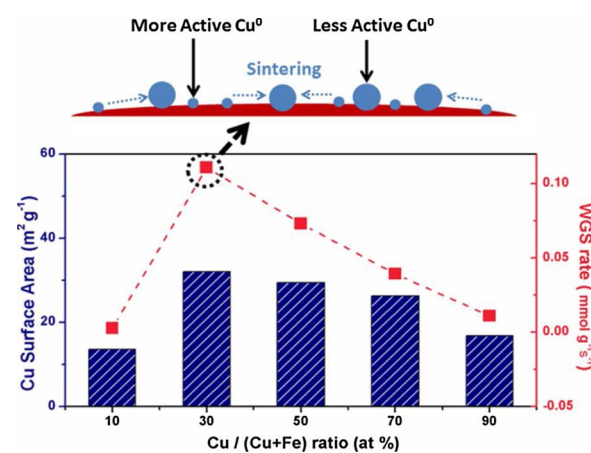


Fig. 12. Variation trend of Cu surface area (blue) and WGS reaction rate (red) with Cu content of $\text{Cu}-\text{Fe}_3\text{O}_4$ catalysts (Reaction temperature: 250 °C), and the microcosmic sketch map of Cu (blue) on the surface of catalysts. (For interpretation of the references to colour in this figure legend, the reader is referred to the web version of this article.)

5. Conclusions

In summary, we have prepared promoted Cu-Fe₃O₄ catalysts for WGS reaction. ASSA turns out to be an excellent preparation method for bulk catalysts with tuned compositions and uniform morphology. The Cu-Fe₃O₄ and Cu-Fe₃O₄-Al₂O₃ show outstanding WGS activity. The Fe addition largely improves the dispersion of Cu⁰, which results in better reducibility because of the pronounced Cu-Fe interaction. In turn, Cu-Fe₃O₄ catalysts exhibit enhanced CO and CO₂ adsorption. The Fe₃O₄ component also facilitates the adsorption of H₂O. All of these effects by the Fe addition result in the great promotion of activity towards WGS reaction.

We have discovered a volcano curve of WGS activity toward Cu concentration in Cu-Fe₃O₄ catalysts, which suggests the importance in optimization of Cu amount. Excessive amount of Cu under WGS conditions results in sintering and deactivation. Catalysts with low Cu concentration suffer from insufficient Cu active phases and CO poisoning, ending up with low LTS activity.

Though the Fe component can significantly disperse Cu and promote WGS activity, long-term stability tests have shown that the durability for Cu-Fe₃O₄ catalysts at 250 °C is poor. The development of tri-component Cu-Fe₃O₄-Al₂O₃ catalyst can solve the corresponding problem and shows promising prospect.

Conflict of interest

The authors declare no competing financial interest.

Acknowledgment

This work is financially supported from the Excellent Young Scientists Fund from National Science Foundation of China (NSFC, grant nos. 21622106), other projects from the NSFC (grant nos. 21501109, 21771117), the Taishan Scholar Project of Shandong Province (China), China Postdoctoral Science Foundation (2014M551891 and 2015T80706), the Outstanding Young Scholar Fund from Science Foundation of Shandong Province of China (JQ201703) and Postdoctoral Innovation Project Foundation of Shandong Province of China (201301008).

Appendix A. Supplementary data

Supplementary data associated with this article can be found, in the online version, at <https://doi.org/10.1016/j.apcatb.2017.12.050>.

References

- [1] J.J. Spivey, Catal. Today 100 (2005) 171–180.
- [2] C. Ratnasamy, J.P. Wagner, Catal. Rev. Sci. Eng. 51 (2009) 325–440.
- [3] M. Zhu, I.E. Wachs, ACS Catal. 6 (2016) 722–732.
- [4] M. Yang, J. Liu, S. Lee, B. Zugic, J. Huang, L.F. Allard, M. Flytzani-Stephanopoulos, J. Am. Chem. Soc. 137 (2015) 3470–3473.
- [5] M. Yang, S. Li, Y. Wang, J.A. Herron, Y. Xu, L.F. Allard, S. Lee, J. Huang, M. Mavrikakis, M. Flytzani-Stephanopoulos, Science 346 (2014) 1498–1501.
- [6] M. Yang, L.F. Allard, M. Flytzani-Stephanopoulos, J. Am. Chem. Soc. 135 (2013) 3768–3771.
- [7] R. Kam, C. Selomulya, R. Amal, J. Scott, J. Catal. 273 (2010) 73–81.
- [8] Y. Li, Q. Fu, M. Flytzani-Stephanopoulos, Appl. Catal. B 27 (2000) 179–191.
- [9] N.A. Koryabkina, A.A. Phatak, W.F. Ruetttinger, R.J. Farrauto, F.H. Ribeiro, J. Catal. 217 (2003) 233–239.
- [10] C.T. Campbell, K.A. Daube, J. Catal. 104 (1987) 109–119.
- [11] J. Nakamura, J.M. Campbell, C.T.J. Campbell, Chem. Soc. Faraday Trans. 86 (1990) 2725–2734.
- [12] H. Yahirō, K. Murawaki, K. Saiki, T. Yamamoto, H. Yamaura, Catal. Today 126 (2007) 436–440.
- [13] R. Si, J. Raitano, N. Yi, L. Zhang, S. Chan, M. Flytzani-Stephanopoulos, Catal. Today 180 (2012) 68–80.
- [14] H. Yahirō, K. Nakaya, T. Yamamoto, K. Saiki, H. Yamaura, Catal. Commun. 7 (2006) 228–231.
- [15] M.N. Moreira, A.M. Ribeiro, A.F. Cunha, A.E. Rodrigues, M. Zabilskiy, P. Djinovic, A. Pintar, Appl. Catal. B 189 (2016) 199–209.
- [16] C.-S. Chen, W.-H. Cheng, S.-S. Lin, Appl. Catal. A 257 (2004) 97–106.
- [17] C.-S. Chen, W.-H. Cheng, S.-S. Lin, Appl. Catal. A 238 (2003) 55–67.
- [18] L. Li, Y. Zhan, Q. Zheng, Y. Zheng, X. Lin, D. Li, J. Zhu, Catal. Lett. 118 (2007) 91–97.
- [19] E.T. Saw, U. Oemar, X.R. Tan, Y. Du, A. Borgna, K. Hidajat, S. Kawi, J. Catal. 314 (2014) 32–46.
- [20] J. Kugai, J.T. Miller, N. Guo, C. Song, J. Catal. 277 (2011) 46–53.
- [21] J. Kugai, J.T. Miller, N. Guo, C. Song, Appl. Catal. B 105 (2011) 306–316.
- [22] A. Kaftan, M. Kusche, M. Laurin, P. Wasserscheid, J. Libuda, Appl. Catal. B 201 (2017) 169–181.
- [23] C.-S. Chen, T.-W. Lai, C.-C. Chen, J. Catal. 273 (2010) 18–28.
- [24] M. Estrella, L. Barrio, G. Zhou, X. Wang, Q. Wang, W. Wen, J.C. Hanson, A.I. Frenkel, J.A. Rodriguez, J. Phys. Chem. C 113 (2009) 14411–14417.
- [25] J.L.C. Fajín, M.N.D.S. Cordeiro, H.R.B. Gomes, Appl. Catal. B 218 (2017) 199–207.
- [26] H. Yahirō, K. Sagata, T. Yamamoto, K. Saiki, M. Asamoto, H. Yamaura, Catal. Lett. 124 (2008) 233–237.
- [27] K. Sagata, N. Imazu, H. Yahirō, Catal. Today 201 (2013) 145–150.
- [28] N. Thouchprasitchai, A. Luengnaruemitchai, S. Pongstabodee, J. Ind. Eng. Chem. 19 (2013) 1483–1492.
- [29] X. Lin, R. Li, Y. Zhang, Y. Zhan, C. Chen, Q. Zheng, J. Ma, Int. J. Hydrot. Energy 40 (2015) 1735–1741.
- [30] X. Lin, Y. Zhang, L. Yin, C. Chen, Y. Zhan, D. Li, Int. J. Hydrot. Energy 39 (2014) 6424–6432.
- [31] H.-C. Wu, T.-C. Chen, J.H. Wu, C.-H. Chen, J.-F. Lee, C.-S. Chen, Catal. Sci. Technol. 6 (2016) 6087–6096.
- [32] S. Natesakawat, X. Wang, L. Zhang, U.S. Ozkan, J. Mol. Catal. A: Chem. 260 (2006) 82–94.
- [33] L. Zhang, X. Wang, J.M. Millet, P.H. Matter, U.S. Ozkan, Appl. Catal. A: Gen. 351 (2008) 1–8.
- [34] L. Zhang, J.M. Millet, U.S. Ozkan, Appl. Catal. A: Gen. 357 (2009) 66–72.
- [35] P. Gawade, B. Mirkelamoglu, B. Tan, U.S. Ozkan, J. Mol. Catal. A: Chem. 321 (2010) 61–70.
- [36] H.-S. Na, D.-W. Jeong, W.-J. Jang, J.-O. Shim, H.-S. Roh, Int. J. Hydrot. Energy 40 (2015) 12268–12274.
- [37] Z. Bao, W. Ding, Q. Li, Int. J. Hydrot. Energy 37 (2012) 951–955.
- [38] V. Subramanian, E.S. Gnanakumar, D.W. Jeong, W.B. Han, C.S. Gopinath, H.S. Roh, Chem. Commun. 49 (2013) 11257–11259.
- [39] S. Kameoka, T. Tanabe, A.P. Tsai, Catal. Lett. 100 (2005) 89–93.
- [40] X. Lin, Y. Zhang, L. Yin, J. Fuel Chem. Technol. 42 (2014) 1087–1092.
- [41] X. Fu, Q. Shen, D. Shi, K. Wu, Z. Jin, X. Wang, R. Si, Q. Song, C. Jia, C. Yan, Appl. Catal. B 211 (2017) 176–187.
- [42] L. Kuai, J.X. Wang, T. Ming, C.H. Fang, Z.H. Sun, B.Y. Geng, J.F. Wang, Sci. Rep. 5 (2015) 9923.
- [43] H. Yan, Y. Xu, Y. Gu, H. Li, X. Wang, Z. Jin, S. Shi, R. Si, C. Jia, C. Yan, J. Phys. Chem. C 120 (2016) 7685–7696.
- [44] C.J.G. Van Der Grint, A.F.H. Wielers, B.P.J. Jogh, J. Van Beunum, M. De Boer, M. Versluijs-Helder, J.W. Geus, J. Catal. 131 (1991) 178–189.
- [45] Z.L. Yuan, L.N. Wang, J.H. Wang, S.X. Xia, P. Chen, Z.Y. Hou, X.M. Zheng, Appl. Catal. B 101 (2011) 431–440.
- [46] P. Panagiotopoulou, D.I. Kondarides, J. Catal. 225 (2004) 327–336.
- [47] C.K. Tsung, J. Fan, N. Zheng, Q. Shi, A.J. Forman, J. Wang, G.D. Stucky, Angew. Chem. Int. Ed. 47 (2008) 8682–8686.
- [48] L. Kuai, J. Geng, C. Chen, E. Kan, Y. Liu, Q. Wang, B. Geng, Angew. Chem. Int. Ed. 53 (2014) 7547–7551.
- [49] G. Munteanu, L. Ilieva, D. Andreeva, Thermochim. Acta 291 (1997) 171–177.
- [50] A. Khan, P.G. Smirniotis, J. Mol. Catal. A: Chem. 280 (2008) 43–51.
- [51] G.C. de Araujo, M. do, C. Rangel, Catal. Today 62 (2000) 201–207.
- [52] M.F. Luo, J.M. Ma, J.Q. Lu, Y.P. Song, Y.J. Wang, J. Catal. 246 (2007) 52–59.
- [53] K. Hadjiiivanov, H. Knozinger, Phys. Chem. Chem. Phys. 3 (2001) 1132–1137.
- [54] T. Tabakova, F.B. Bocciuzzi, M. Manzoli, D. Andreeva, Appl. Catal. A 252 (2003) 385–397.
- [55] E. Fiolitakis, H. Hofmann, J. Catal. 80 (1983) 328–339.
- [56] D.S. Newsome, Catal. Rev. Sci. Eng. 21 (1980) 275–318.
- [57] J.M. Trillo, G. Munuera, J.M. Criado, Catal. Rev. 7 (1972) 51–86.
- [58] M. Ai, J. Catal. 50 (1977) 291–300.
- [59] Y. Ye, L. Wang, S. Zhang, Y. Zhu, J. Shan, F. Tao, Chem. Commun. 49 (2013) 4385–4387.
- [60] K.M.K. Yu, C.M.Y. Yeung, S.C. Tsang, J. Am. Chem. Soc. 129 (2007) 6360–6361.
- [61] S.D. Jones, L.M. Neal, H.E. Hagelin-Weaver, Appl. Catal. B 84 (2008) 631–642.
- [62] B. Lorenzut, T. Montini, L.D. Rogatis, P. Canton, A. Benedetti, P. Fornasiero, Appl. Catal. B 101 (2011) 397–408.
- [63] G. Corro, S. Cebada, U. Pal, J.L.G. Fierro, L. Alvarado, Appl. Catal. B 165 (2015) 555–565.